minerals

MDPI

Article

Garnet-Vesuvianite Equilibrium in Rodingites from Dobšiná (Western Carpathians)

Juraj Butek [1,2,*], Ján Spišiak [1] and Stanislava Milovská [3]

[1] Faculty of Natural Sciences, Matej Bel University, Tajovského 40, 97400 Banská Bystrica, Slovakia; jan.spisiak@umb.sk
[2] Géosciences Environnement Toulouse, Université de Toulouse, UPS, CNRS-IRD-CNES, 14 Av. E. Belin, 31400 Toulouse, France
[3] Earth Science Institute of the Slovak Academy of Sciences, Ďumbierska 1, 97401 Banská Bystrica, Slovakia; milovska@savbb.sk
* Correspondence: juraj.butek@umb.sk

Abstract: Intensively metasomatized rocks from serpentinized ultramafic tectonic fragments in Dobšiná, Western Carpathians, consist of typical rodingite mineral association: hydrated garnet, vesuvianite, diopside and clinochlore. Electron microprobe analysis (EMPA) and Micro-Raman analyses of the main minerals evidence complex mineralogical evolution and variable mineral chemistry. Garnet solid solution is dominated by grossular-andradite series, which demonstrates a significant degree of hydration, mainly for grossular rich garnet cores. Garnet is locally enriched in TiO_2 (up to 13 wt%), possibly indicating a chemical relic of a Ti-oxide mineral. Younger, andradite-richer garnet rims demonstrate a low degree of hydration, suggesting a harder incorporation of an $(OH)^-$ anion into its crystal structure. Garnet chemical variations display an ideal negative correlation between Al and (Fe^{3+} + Ti). The most recent mineral phase is represented by euhedral vesuvianite (± chlorite), which crystallizes at the expense of the garnet solid solution. This reaction shows a well-equilibrated character and indicates a high extent of rodingitization process. Chlorite thermometry models suggest an average temperature of late rodingite (trans) formation of about 265 °C.

Keywords: rodingite; hydrogrossular; garnet; vesuvianite; micro-Raman spectra; Dobšiná

Citation: Butek, J.; Spišiak, J.; Milovská, S. Garnet-Vesuvianite Equilibrium in Rodingites from Dobšiná (Western Carpathians). *Minerals* **2021**, *11*, 189. https://doi.org/10.3390/min11020189

Academic Editor: Evgeny Galuskin
Received: 7 December 2020
Accepted: 6 February 2021
Published: 11 February 2021

1. Introduction

Rodingite represents a particular calcium-rich metasomatic rock. Its formation is closely related to the serpentinization process of ultramafic rocks since the origin of the metasomatic fluid is generally regarded as a product of serpentinization [1–6]. These rocks are characterized by a heterogeneous and quite complex mineralogy, mostly dominated by Ca-rich often hydrated silicate minerals: garnet, vesuvianite, diopside, chlorite, epidote, zoisite, tremolite, prehnite and others [7–11]. Rodingites have been disregarded for a long time probably because of their heterogeneous and altered character, but they have recently been recognized as a source of information on fluid compositions and their circulation in both ocean floor and subduction zones [12–15].

Furthermore, the specific mineralogy allows us to analyze the rather rare chemistry and crystallography of certain mineral phases. Garnet with a general structural formula of $X_3Y_2Z_3O_{12}$ is described from various geological settings and represents probably the most chemically variable mineral in Earth's crust [16]. In the case of rodingites, garnet is additionally often hydrated (incorporation of OH component), which substantially complicates its crystal structure [17–19]. Similarly, vesuvianite represents a typical rodingite mineral and its complex sorosilicate structure [20] allows to incorporate relatively uncommon elements such as As, B, Be, Cu or others [21–23].

In this study, we report an equilibrated crystallization of vesuvianite at the expense of a complex garnet solid solution in rodingite from Dobšiná, Western Carpathians. The aim of this work is to document the mineralogical evolution and to discuss the formation of these metasomatic rocks.

2. Geological Background

The Carpathian Mountains, located in central and eastern Europe, represent a 1500 km long part of the Alpine Orogenic belt formed by a series of Jurassic to Tertiary subduction and collision events. The geology of this mountain range is, similar to the structure of the Alps, characterized by a complicated structure with numerous thrust faults and nappes [24]. The Western Carpathians, situated mostly in Slovakia, can be longitudinally divided into three main tectonic zones: External, Central and Internal Western Carpathians [25,26]. The Central Western Carpathians form the core of the Carpathian Orogeny and can be subdivided, on the basis of major thick-skinned thrust sheets, into the Core mountains Belt, the Vepor Belt and the Gemer Belt (Figure 1a). The Gemeric unit, the main tectonic unit of the Gemer Belt, is composed mainly of low-grade metamorphic rocks of the Paleozoic age. This unit is overlain by several Mesozoic thin-skinned nappe units belonging to the Internal Western Carpathians. One of these, the Meliata unit, represents evidence of the Meliata (Meliata–Hallstatt) ocean domain which closed during the Middle to Upper Jurassic [26–28]. Relics of this ocean domain are formed of blueschist-facies metamorphic rocks and a mélange of sedimentary and volcanic rocks, all of them irregularly dispersed as a discontinuous nappe unit overlying the Gemeric unit.

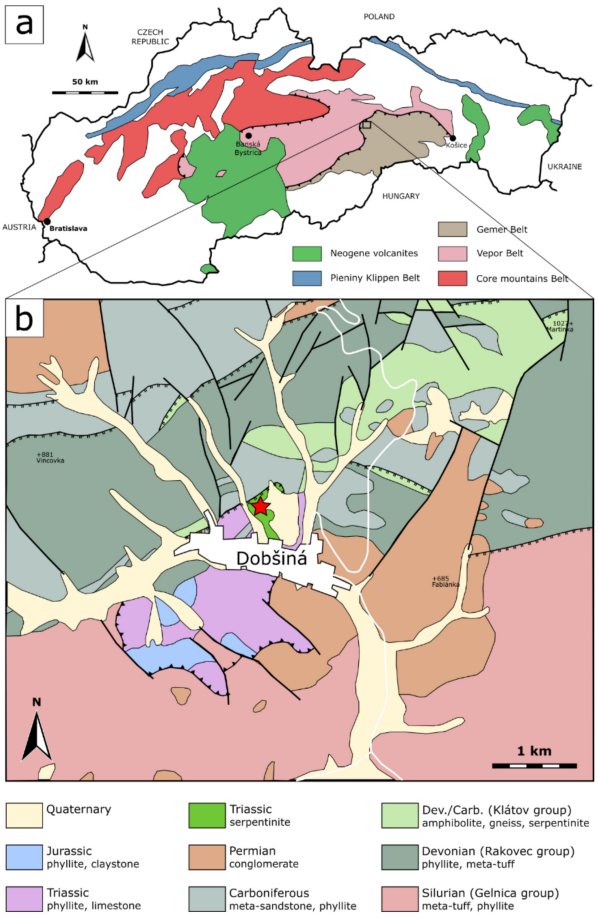

Figure 1. (**a**) Geological sketch map of the Western Carpathians in Slovakia; (**b**) Simplified geological map of Dobšiná region (modified after [29]). The red star denotes the rodingite occurrence.

Two different types of serpentinized ultramafic rock occur in the region of Dobšiná (Figure 1b). The first type is associated with relatively scarce high-grade metamorphic rocks (amphibolite–gneiss series) belonging to the Klátov group of the Early Paleozoic Gemeric basement [30]. The second type, occurring in the north of Dobšiná town (N48°49′43.3″ E20°21′56.2″), contains about 1% of chrysotile asbestos that was intensively quarried during the 20th century. This lizardite-chrysotile serpentinite body had (before the exploitation) a tabular/lens-shaped form with dimensions of about 700 × 200–500 m and a maximal thickness of about 45 m. Along with lizardite and chrysotile, the serpentinite rarely contains relics of primary minerals such as olivine, pyroxenes and brown Cr-spinel [31]. The locality is also well-known for the occurrence of yellow–green Cr-rich andradite (demantoid variety); [32]. Underlying sedimentary sequences are represented by the Lower Triassic marls, schists, and marl limestones of the Olenekian age. Overlying rocks are represented by massive Middle Triassic carbonates [31]. The serpentinite body is intensively disintegrated, and along with occurring rocks including talc–phengite–glaucophane schists, marbles, metaconglomerates and blueschists, it probably represents a tectonic fragment of an accretionary wedge "mélange" complex belonging to the Meliata unit [33].

Massive, light-gray aphanitic rocks identified as rodingites were collected in the northern part of the quarry already in the late 1970s (Figure 1b). Rodingites were cropped out as an about 2 m thick sheet-like body with a dark 1–2 cm thick chlorite reaction rim [31]. These reaction rims and less altered harzburgite zones were characterized by the occurrence of perovskite. This occurrence has been studied in detail by Putiš et al. [33,34] and Li et al. [35]. Perovskite crystals are locally replaced by Ti-rich (up to 14 wt% of TiO_2) andradite garnet. U-Pb dating of the perovskites allowed the determination of the age of serpentinization and rodingitization processes to 150–130 Ma.

3. Materials and Methods

Electron microscopy and Wavelength-dispersive spectroscopy (WDS) microprobe analyses of rodingite minerals were carried out from classic thin sections using a JEOL JSM-6360LV coupled with SDD Bruker 129 eV operated at the Earth Science Institute of the Slovak Academy of Science, Banská Bystrica, Slovakia. Measurements were performed using an accelerating voltage 15 keV, current 20 nA, spot size 2–5 μm, ZAF correction, counting time 10 s on peak and 5 s on background. Standards set consisted of Ca (Kα, 25)-diopside; K (Kα, 44)-orthoclase; Na (Kα, 43)-albite; Mg (Kα, 41)-diopside; Al (Kα, 42)-albite; Si (Kα, 63)-quartz; Fe (Kα, 52)-hematite; Cr (Kα, 113)-Cr_2O_3; Mn (Kα, 59)-rhodonite; V (Lα, 122)-ScVO4; Y (Lα, 122)-YPO_4; Ti (Kα, 130)-rutile; spectral lines and detection limits in ppm are in parentheses.

The processing of garnet microprobe analyses and the recalculation of mineral formula were complicated by the presence of OH in the crystal structure and probably both iron oxidation states (Fe^{2+} and Fe^{3+}). The H_2O content in garnets was calculated from the deficiency of Si in the tetrahedral site ($Si^{4+} + H^+/4 = 3$) after normalization on 8 cations (including H^+), considering all iron to be Fe^{3+}. Vesuvianite formula recalculation was based on 50 cations and 78 anions, considering all iron to be Fe^{3+}. Pyroxenes were recalculated using a common normalization procedure on 6 oxygen atoms. The recalculation of chlorite analyses and chlorite thermometry were performed using WinCcac software from Yavuz et al. [36]. Graphical representations of microprobe results were made using Golden Software Grapher.

The unpolarized Raman spectroscopic measurements of thin sections were performed on a Labram HR800 microspectrometer (Horiba Jobin-Yvon), based on the Olympus BX41 microscope with a confocally coupled Czerny-Turner type monochromator (focal length 800 mm) operating at the Earth Science Institute of the Slovak Academy of Science, Banská Bystrica, Slovakia. A frequency-doubled Nd-YAG laser at 532 nm (torus 532, Laser Quantum, UK) was used for excitation. The Raman-scattered light was collected in 180° geometry through a 100× objective lens with numerical aperture 0.8 and dispersed by diffraction grating with 600 grooves per mm onto a cooled charge-coupled device (CCD) detector,

with a total exposure time of 180 s. Selected points spectra were acquired in the range of 100–1200 and 2900–4000 cm^{-1} in order to identify the presence of hydroxyl anion in the structure. The system resolution was less than 6 cm^{-1}, and band definition was improved using 2-fold sub-pixel shift. The grating turret accuracy was calibrated between the zero-order line and the laser line at 0 cm^{-1}. Spectral accuracy was verified on the 734 cm^{-1} band of Teflon.

4. Results

4.1. Petrography

Thin section observations showed that rodingites are characterized by an irregular distribution of the main mineral phases, which include garnet, vesuvianite, clinopyroxene and chlorite (Figure 2). The rock is mainly made up by anhedral garnet representing an amber-colored matrix (Figure 2a) occasionally showing anomalous anisotropic optical features (typical for hydrated garnets). Electron microscopy observations confirmed that the rocks are very heterogeneous, with a locally well-defined core-rim zonation (Figures 3 and 4a). Vesuvianite occurs mainly in the form of euhedral and colorless crystals, which are concentrated especially in the veins and in the clusters, but it is also present in well-crystallized forms within the garnet matrix (Figures 2b, 3a and 4b). Euhedral vesuvianite is frequently observed as overgrown around the relatively recent garnet rims (Figure 3a). The clinopyroxene grains are altered and irregular (relics), while the only alteration product is represented by chlorite. Chlorite additionally forms locally bigger crystal clusters in association with euhedral vesuvianite.

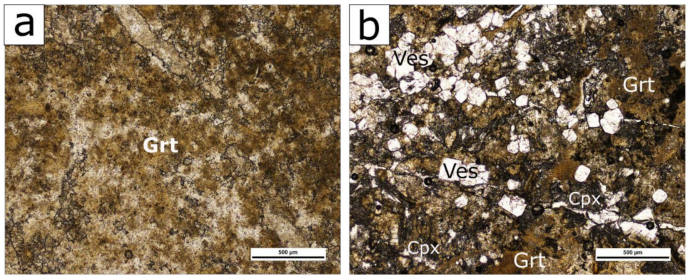

Figure 2. Microphotographs of rodingite samples from Dobšiná; (**a**) Heterogenous garnet solid solution, plane polarized light. (**b**) Main mineral assemblage consisting of clinopyroxene relics, heterogenous garnet matrix and well-crystallized colorless crystals of vesuvianite, plane polarized light. Ves—vesuvianite; Grt—garnet; Cpx—clinopyroxene.

Table 1. Representative electron-microprobe composition (wt%) of garnet solid solution from Dobšiná.

	Figure 2			Figure 4a			Figure 4b						
	Grs 1	**Adr 1**	**Adr 2**	**Grs 2**	**Adr 3**	**Adr 4**	**Grs 3**	**Ti-Grt 1**	**Ti-Grt 2**	**Grs**	**Adr**	**Ti-Grt**	**Ti-Grt**
SiO_2	32.46	37.32	35.95	30.94	37.01	36.08	31.62	34.46	33.82	31.34	36.30	32.71	33.34
TiO_2	0.16	1.33	1.04	1.89	2.11	1.43	2.24	8.14	10.20	1.40	1.19	12.36	10.56
Al_2O_3	21.24	13.80	6.17	20.62	13.95	8.50	20.87	10.03	9.18	20.83	8.94	6.91	8.98
Cr_2O_3	0.00	0.01	0.00	0.00	0.01	0.07	0.00	0.00	0.00	0.00	0.00	0.01	0.03
V_2O_3	0.00	0.06	0.08	0.02	0.07	0.07	n.a.	n.a.	n.a.	0.01	0.02	n.a.	n.a.
Y_2O_3	0.01	0.01	0.01	0.01	0.02	0.00	n.a.	n.a.	n.a.	0.01	0.00	n.a.	n.a.
FeO_{total}	2.00	9.90	19.07	1.57	9.53	16.14	1.42	9.56	8.77	1.61	15.91	9.13	8.64
MnO	0.08	0.04	0.13	0.02	0.00	0.13	0.06	0.12	0.22	0.00	0.12	0.17	0.21
MgO	0.00	0.00	0.09	0.00	0.02	0.02	0.03	0.09	0.32	0.01	0.02	0.56	0.28
CaO	37.84	36.23	34.46	38.13	36.28	35.09	38.84	36.38	35.90	37.83	35.29	35.93	35.93
Na_2O	0.03	0.02	0.00	0.00	0.00	0.06	0.01	0.00	0.02	0.00	0.00	0.00	0.01
Total	93.86	98.72	97.00	93.21	99.02	97.61	95.09	98.77	98.43	93.06	97.80	97.80	97.97
H_2O*	4.81	0.83	0.47	5.87	1.15	0.84	5.94	2.77	3.10	5.48	0.78	3.61	3.35

Table 1. *Cont.*

	Figure 2			Figure 4a			Figure 4b						
	Grs 1	**Adr 1**	**Adr 2**	**Grs 2**	**Adr 3**	**Adr 4**	**Grs 3**	**Ti-Grt 1**	**Ti-Grt 2**	**Grs**	**Adr**	**Ti-Grt**	**Ti-Grt**
*H_2O calculated on Si deficiency tetrahedral position; formula normalized on 8 cations (including H^+), Fe_{total} calculated as Fe^{3+}													
Si^{4+}	2.40	2.89	2.94	2.28	2.85	2.89	2.28	2.65	2.60	2.32	2.90	2.53	2.57
$H^+/4$	0.59	0.11	0.06	0.72	0.15	0.11	0.72	0.35	0.40	0.68	0.10	0.47	0.43
Σ *Z*	3.00	3.00	3.00	3.00	3.00	3.00	3.00	3.00	3.00	3.00	3.00	3.00	3.00
Ti^{4+}	0.01	0.08	0.06	0.10	0.12	0.09	0.12	0.47	0.59	0.08	0.07	0.72	0.61
Al^{3+}	1.85	1.26	0.59	1.79	1.27	0.80	1.78	0.91	0.83	1.82	0.84	0.63	0.82
Cr^{3+}	0.00	0.00	0.00	0.00	0.00	0.00	0.00	0.00	0.00	0.00	0.00	0.00	0.00
V^{3+}	0.00	0.00	0.00	0.00	0.00	0.00				0.00	0.00		
Y^{3+}	0.00	0.00	0.00	0.00	0.00	0.00				0.00	0.00		
Fe^{3+}	0.12	0.64	1.30	0.10	0.61	1.08	0.09	0.61	0.56	0.10	1.06	0.59	0.56
Mn^{2+}	0.00	0.00	0.01	0.00	0.00	0.01	0.00	0.01	0.01	0.00	0.01	0.01	0.01
Mg^{2+}	0.00	0.00	0.01	0.00	0.00	0.00	0.00	0.01	0.04	0.00	0.00	0.06	0.03
Σ *Y*	1.99	1.99	1.98	1.99	2.01	1.98	1.99	2.01	2.04	2.00	1.98	2.02	2.03
Ca^{2+}	3.00	3.01	3.02	3.01	2.99	3.01	3.01	2.99	2.96	3.00	3.02	2.98	2.97
Na^+	0.00	0.00	0.00	0.00	0.00	0.01	0.00	0.00	0.00	0.00	0.00	0.00	0.00
Σ *X*	3.01	3.01	3.02	3.01	2.99	3.02	3.01	2.99	2.96	3.00	3.02	2.98	2.97

n.a. = not analyzed.

Table 2. Representative electron-microprobe compositions (wt%) of vesuvianites, clinopyroxenes and chlorites from Dobšiná.

	Ves 1	**Ves 2**	**Ves 3**	**Ves**	**Ves**	**Cpx 1**	**Cpx 2**	**Cpx**	**Chl**	**Chl**	**Chl**
SiO_2	36.84	36.77	36.87	36.93	36.48	55.21	53.76	55.15	31.13	31.34	30.23
TiO_2	1.14	1.23	1.04	1.05	1.09	0.03	0.09	0.03	0.00	0.00	0.00
Al_2O_3	15.70	15.89	15.70	14.99	15.65	0.00	1.49	0.05	17.42	17.39	17.69
Cr_2O_3	0.03	0.02	0.08	0.00	0.00	0.01	0.00	0.00	0.00	0.00	0.07
FeO_{total}	2.93	3.07	3.76	4.18	2.59	1.51	6.49	2.90	6.84	4.85	8.58
MnO	0.11	0.16	0.09	0.07	0.09	0.29	0.19	0.33	0.27	0.33	0.35
MgO	3.05	2.85	3.00	3.28	3.05	17.88	13.27	16.65	29.95	31.15	29.16
CaO	36.32	35.93	36.44	36.47	36.09	25.95	23.78	25.82	0.09	0.03	0.01
Na_2O	0.03	0.02	0.00	0.00	0.00	0.02	0.69	0.02	0.00	0.04	0.01
K_2O	n.a.	n.a.	0.00	0.00	n.a.	n.a.	n.a.	0.00	0.02	0.01	0.02
Total	96.21	95.97	97.00	97.00	95.10	100.95	99.81	100.96	85.71	85.15	86.12
H_2O	2.73	2.63	2.74	2.80	2.72				12.31	12.36	12.24
Fe_2O_3	3.26	3.42	4.18	4.64	2.88				0.00	0.00	0.32
	formula normalized on 50 cations and 78 anions, Fe_{total} calculated as Fe^{3+}					formula normalized on 6 oxygens			formula normalized on 10 oxygens and 8 $(OH)^-$		
Si^{4+}	18.00	18.03	17.90	17.94	18.02	1.99	1.99	2.00	3.03	3.04	2.96
Ti^{4+}	0.42	0.45	0.38	0.38	0.41	0.00	0.00	0.00	0.00	0.00	0.00
Al^{3+}	9.04	9.18	8.99	8.58	9.11	0.00	0.06	0.00	2.00	1.99	2.04
Cr^{3+}	0.01	0.01	0.03	0.00	0.00	0.00	0.00	0.00	0.00	0.00	0.01
Fe^{2+}						0.05	0.20	0.09	0.56	0.39	0.68
Fe^{3+}	1.20	1.26	1.53	1.70	1.07				0.00	0.00	0.02
Mn^{2+}	0.05	0.07	0.04	0.03	0.04	0.01	0.01	0.01	0.02	0.03	0.03
Mg^{2+}	2.22	2.08	2.17	2.37	2.25	0.96	0.73	0.90	4.35	4.51	4.26
Ca^{2+}	19.01	18.88	18.96	18.99	19.10	1.00	0.94	1.00	0.01	0.00	0.00
Na^+	0.03	0.02	0.00	0.00	0.00	0.00	0.05	0.00	0.00	0.01	0.00
K^+			0.00	0.00				0.00	0.00	0.00	0.00
Σ	50	50	50	50	50	4.01	3.99	4.00	9.97	9.97	10.00
$(OH)^-$	8.91	8.61	8.87	9.07	8.96				8	8	8

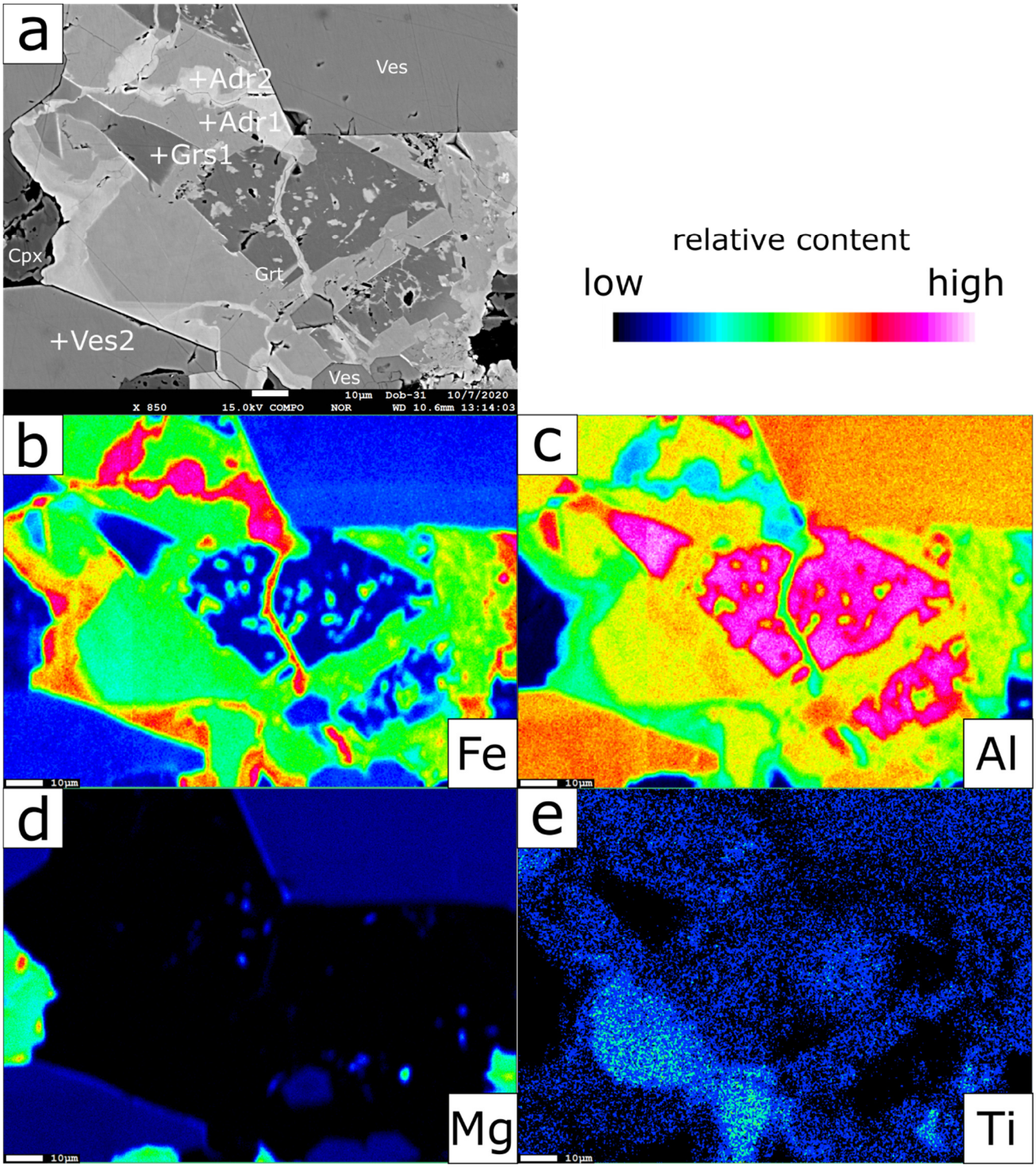

Figure 3. (**a**) BSE (Backscattered electrons) image of the complex garnet solid solution bordered by euhedral vesuvianite. (**b**–**e**) EMPA element distribution maps of Fe, Al, Mg, Ti, respectively. Ves—vesuvianite; Grt—garnet; Adr—andradite; Grs—grossular; Cpx—clinopyroxene. "+" symbol denotes the exact spot analyzed by EMPA (presented in Tables 1 and 2).

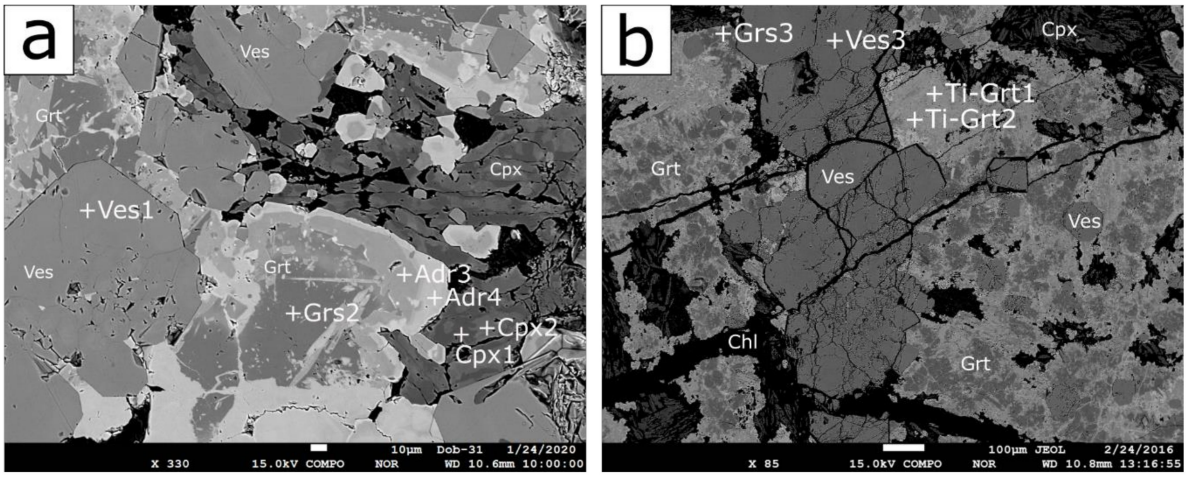

Figure 4. (**a**) BSE image of the complex garnet solid solution and its textural relation to clinopyroxene and euhedral vesuvianite; (**b**) BSE image of the locally Ti-enriched garnet solid solution cut by a later vesuvianite vein. Ves—vesuvianite; Grt—garnet; Adr—andradite; Grs—grossular; Cpx—clinopyroxene; Chl—chlorite.

4.2. Mineral Chemistry

According to SEM chemical analyses, the garnets are the mineral phases showing the largest compositional variations (Table 1 and Supplementary Materials Table S1). The investigated garnets belong to the grossular-andradite series and in some cases show TiO_2 enrichments (up to 13 wt%). Garnet grains with core-rim zonation show a transition from grossular to andradite, i.e., texturally older garnet is mainly grossular in composition (Figure 3b–e). Major oxide contents, calculated through microprobe analysis, are considerably below 100%, and this suggests a significant presence of OH groups in the garnet's structure (Table 1). The amount of H_2O is estimated (see experimental methods for details) to be up to 5.8 wt%. The hydration is more pronounced in the grossular, while andradite seems devoid (or with very low) of OH components. Ti enriched garnet demonstrates a moderate hydration of about 3 wt% H_2O. The calculated structural formulas can be expressed as $Ca_{2.96-3.04}$ $(Al_{0.58-1.89}$ $Fe^{3+}{}_{0.08-1.37}$ $Ti_{0.00-0.76}$ $Mg_{0.00-0.07}$ $Mn^{2+}{}_{0.00-0.02})$ $(Si_{2.28-2.96}$ $\square_{0.04-0.72})$ $[O_{11.28-11.96}$ $(OH)_{0.04-0.72}]$ where $\square$ denotes vacancy. Despite the fact that most garnets are dominated by grossular end-member, for the purpose of this study they are divided into three chemically distinct groups: hydrated grossular garnet (Grs), Ti enriched garnet (Ti-Grt) and low hydrated grossular-andradite garnet (Adr, Figure 5).

The composition of vesuvianite is quite homogeneous, with only minor variations in TiO_2, Al_2O_3, FeO and MgO (Table 2 and Supplementary Materials Table S2). The composition of this complex sorosilicate mineral is often very similar to that of hydrated grossular; the most reliable distinguishing feature is the presence of MgO (about 2–4 wt%) compared to the garnet solid solution that shows very low (or any) MgO content. The simplified average structural formula of vesuvianite can be expressed as $(Ca_{19.00}Na_{0.01})_{\sum 19.01}$ $(Al_{8.90}Mg_{2.28}Fe^{3+}{}_{1.34}Ti_{0.42}Mn^{2+}{}_{0.05}Cr_{0.01})_{\sum 13.00}$ $(SiO_4)_{9.99}(Si_2O_7)_{4.00}$ $O_{1.11}(OH)_{8.94}$, which is consistent with the ideal formula of vesuvianite sensu stricto, where Fe^{3+} dominates the *Y1* crystallographic position [20].

The chemical composition of clinopyroxenes is characterized by low FeO and high CaO and MgO contents (Table 2 and Supplementary Materials Table S3). Irregular variations in FeO cause an evident zonation, but the petrographic character of this mineral does not allow us to distinguish systematic relations (Figure 4a). Projected into Morimoto's [37] discrimination diagram, clinopyroxenes are classified as diopsides (Figure 6). The average structural formula can be expressed as $Ca_{1.00}$ $Mg_{0.88}$ $Fe^{2+}{}_{0.10}$ $Mn^{2+}{}_{0.01}$ $Al_{0.01}$ $Si_{1.99}$ O_6.

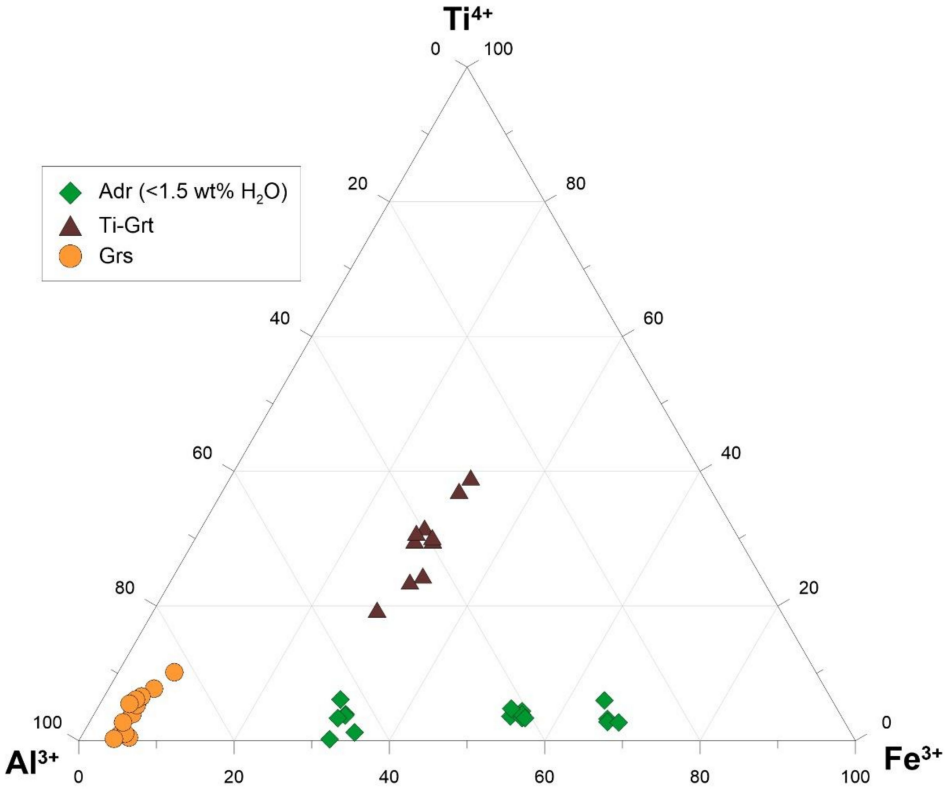

Figure 5. Chemical variations of the garnet solid solution projected into Fe^{3+}-Ti-Al ternary diagram. The low hydrated Adr group represents younger rims of otherwise hydrated garnet cores.

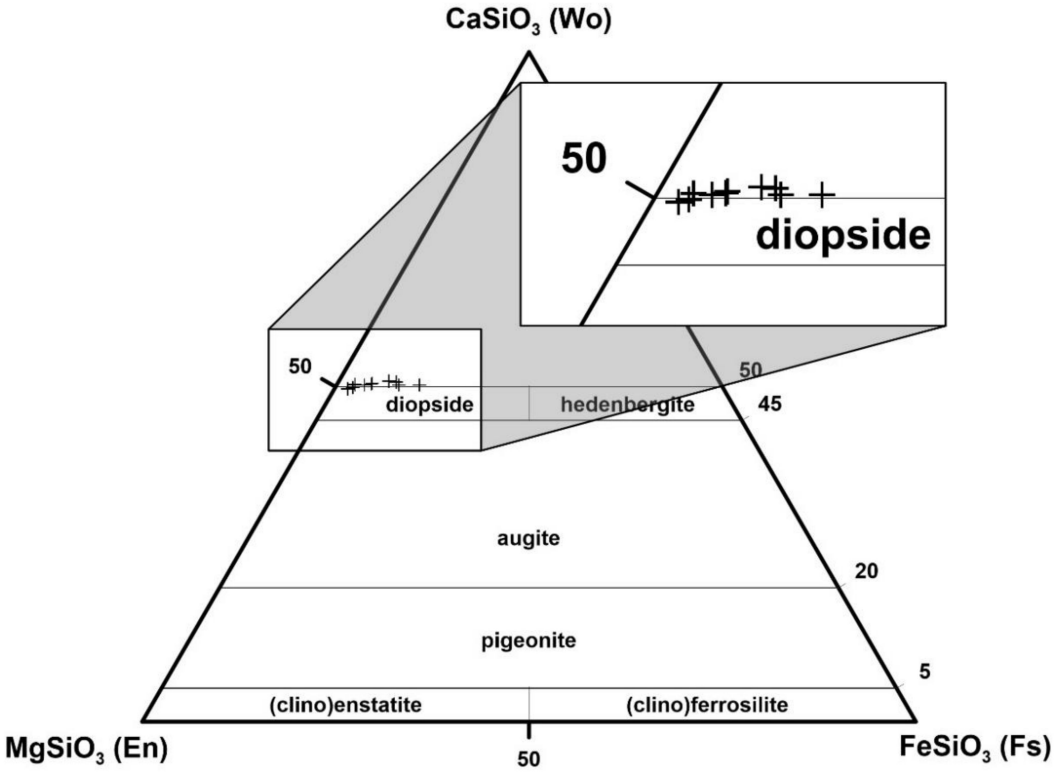

Figure 6. Clinopyroxene analyses projected into Morimoto's [37] discrimination diagram.

The chemical composition of chlorite is characterized by very high contents of MgO with the substantial presence of Al_2O_3 and rather low FeO (Table 2 and Supplementary Materials Table S4). Microprobe analyses show a slightly variable Mg/Fe ratio but, in general, chlorite compositions do not show wide variations. According to all classification schemes used in Yavuz [35], chlorites in rodingites from Dobšiná are clinochlores. Their average structural formula can be expressed as $Mg_{4.42}\ Fe^{2+}{}_{0.51}\ Mn^{2+}{}_{0.02}\ Si_{3.01}\ Al_{2.01}\ O_{10}\ (OH)_8$.

4.3. Raman Spectra

Raman spectra of all studied garnets (Figure 7a–c) in selected chemical zones (see Figures 3 and 4a,b) have vibrational modes at low (below 400 cm^{-1} and in the 400–1015 cm^{-1} region) and at high frequencies (3500–3750 cm^{-1}). Dominant bands occur in regions 350–400 cm^{-1} and 800–900 cm^{-1}. A broad feature in the region of 3500–3750 cm^{-1} with maximum at ~3600 cm^{-1} occurring in all selected points is interpreted as (O-H) stretching modes. Vesuvianite Raman spectra exhibit several weak lines between 100 and 1200 cm^{-1}, dominated by asymmetric bands with higher intensities at 409, 643, 862, and 930 cm^{-1} (Figure 8a). A group of broad bands with low intensity and one dominant sharp line at 3645 cm^{-1} expresses at the Raman shift wavenumbers over 3100 cm^{-1} (Figure 8b). The concurrent luminescent effects are present in all spectra as increased background.

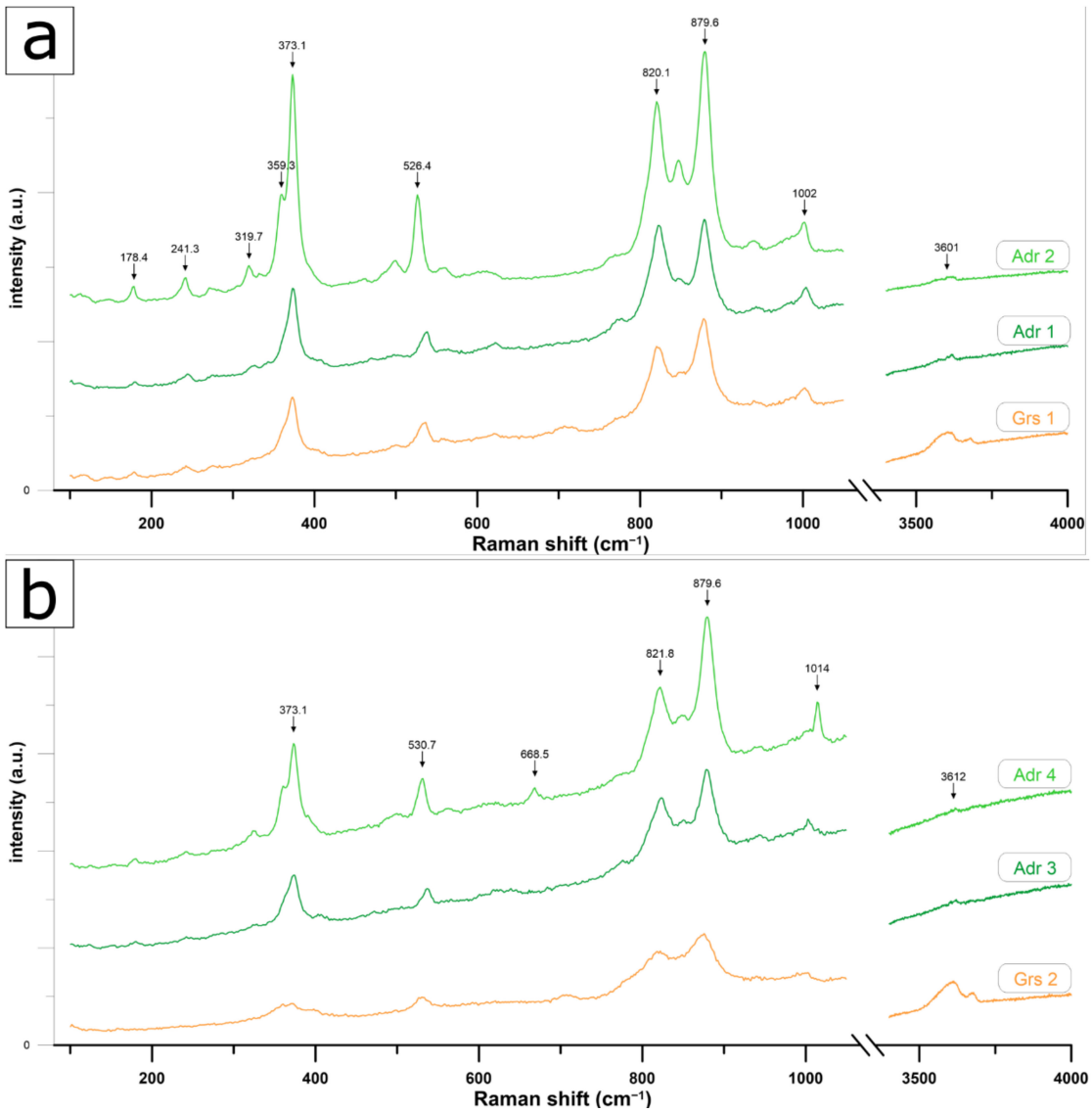

Figure 7. *Cont.*

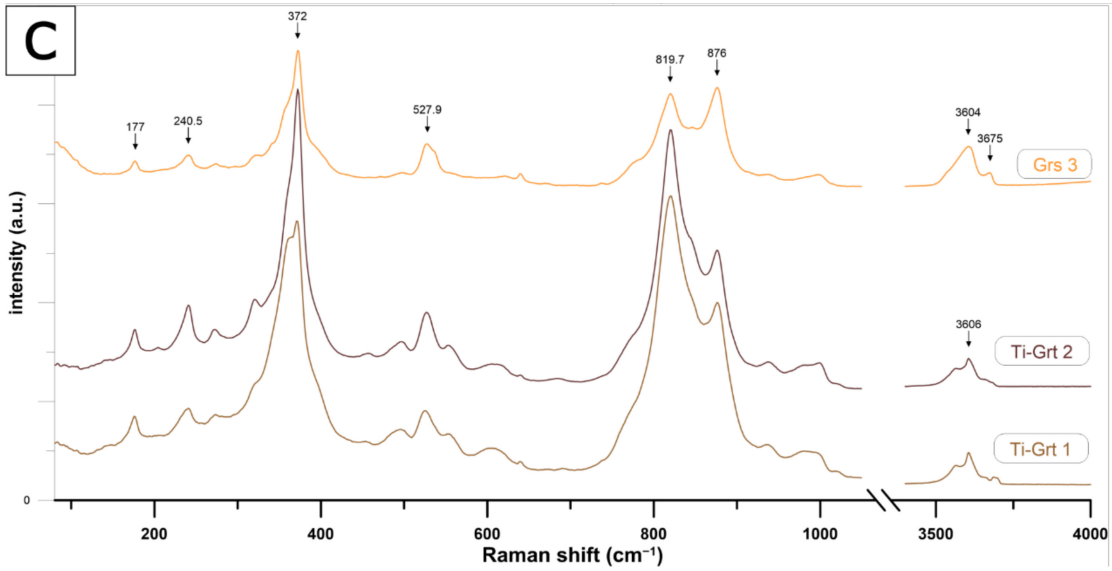

Figure 7. Raman spectra of analyzed garnets demonstrating the different degree of hydration, uncorrected; (**a**) Spectra corresponding to the spots in Figure 3; (**b**) Spectra corresponding to the spots in Figure 4a; (**c**) Spectra corresponding to the spots in Figure 4b.

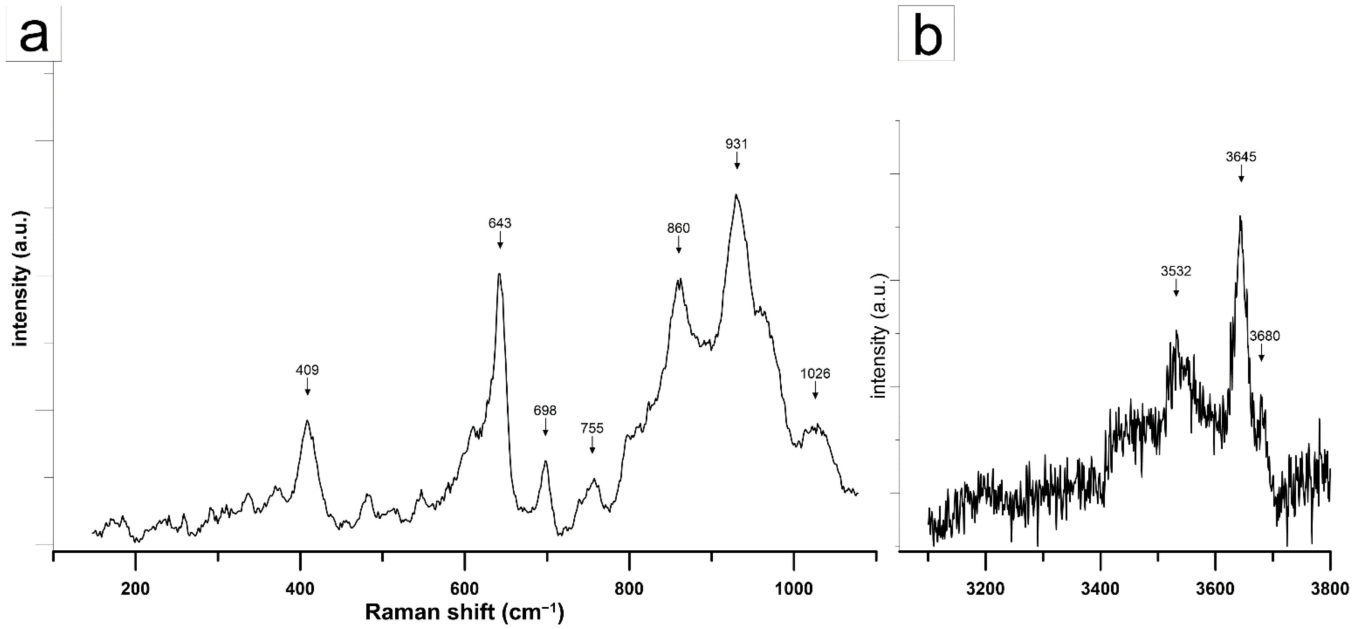

Figure 8. Representative unpolarized Raman spectrum of vesuvianite from Dobšiná; (**a**) Low frequency region, raw spectrum; (**b**) High frequency $(OH)^-$ region, corrected to baseline.

5. Discussion

5.1. Mineralogical Evolution

The mineral composition of rodingite from Dobšiná demonstrates a high extent of metasomatic transformation and complex mineralogical evolution. The chemical signature of diopside relics dominated by very high Ca and Mg contents is in agreement with diopside compositions from rodingites around the world, e.g., [38–40] and confirms its metasomatic origin. As the diopside (possibly with older grossular cores) is considered to be the oldest mineral phase, there are no indications allowing us to discuss the protolith of the rock, although the most often reported protoliths around the world are various mafic magmatic rocks commonly associated with serpentinized bodies, e.g., [3,5,41]. No primary (magmatic) minerals were identified, and contrary to the mineralogy described by Putiš et al. [32], we did not observe Fe-Ti oxides. This can be explained by the fact that

our samples represent more altered/rodingitized parts of this occurrence. Nevertheless, considering the lack of evidence for Ti circulation and the rather restricted mobility of this element in such fluid-dominated environments [42,43], it seems reasonable to suppose that the Ti-rich garnet represents a descendant of a Ti-oxide phase.

Hydrated garnet represents a typical rodingite mineral. This study documents a consistent transition from hydrated grossular to andradite during the rodingite formation. Unhydrated andradite-richer rims therefore represent the last garnet crystallization. Moreover, euhedral vesuvianite apparently crystallizes at the expense of garnet, and the reaction does not seem much influenced by the chemical composition of the garnets since the vesuvianite appears within the heterogeneous garnet solid solution, or in other words, the vesuvianite crystallization affects the grossular cores as well as the andradite rims. Such mineral reaction was proposed by Li et al. [44] based on petrographic observations of metarodingites from Alpine ophiolite: Hgrs + Chl + H_2O = Ves $\pm$ C_m; where "Hgrs" denotes hydrogrossular and "C_m" denotes mobile components, which are predominantly Ca, Na and Si. A similar reaction also illustrating the formation of chlorite clusters in association with the vesuvianite is expressed as: Hgrs + Di + H_2O = Ves + Chl $\pm$ C_m. In general, rodingites from Dobšiná are mineralogically very similar to metarodingites described by Li et al. [44] from Zermatt-Zaas ophiolite, even though their newly formed vesuvianite did not display such a distinct euhedral character. Recently, the reaction Grt $\rightarrow$ Ves was also documented by Micro-Raman mapping performed on rodingites from the Northern Apennines [45]. The physicochemical conditions of this reaction were investigated using multiple thermodynamic modeling approaches [5,44–46]; rather low silica activity and high Ca activity are typically accepted, which is consistent with the composition of rodingitization fluid. The CO_2 fugacity in the fluid was commonly suggested to be rather low [47,48], but the study by Salvioli-Mariani et al. [45] shows that the formation of vesuvianite can occur at higher CO_2 fugacity values as well. In any case, the vesuvianite tends to form at later stages of the rodingitization process and thus represents a higher extent of metasomatic transformation [4,5,12,42,46]. This mineral is abundant in rodingites affected by intense metamorphism [41,42,44,49], but numerous descriptions of rodingites lacking vesuvianite are equally frequent [6,10,39,50–55]. As it is stable over a wide range of temperatures [42,47], the key factor controlling the crystallization of vesuvianite is still not evident and more research is needed on this subject.

Chlorite mineral composition was used to determine the temperature of the most recent vesuvianite + chlorite association. Despite the fact that chlorite thermometry is recommended to be used and interpreted with caution, thermometer models included in Yavuz et al. [36] yielded an average temperature of 265 °C. Spectroscopic measurements of Dobšiná vesuvianite agree with published records of ordered vesuvianites [21,45,56,57] and also confirm the low-temperature origin of this mineral association. Vesuvianite is reliably distinguished from garnet by the peak at 409 cm^{-1} and two broad bands at 860 and 931 cm^{-1}. The broad bands in unpolarized spectra in the region 3100–3750 cm^{-1} with a dominant sharp feature centered at 3645 cm^{-1} and a weak one at ~3680 cm^{-1} also point to low temperature vesuvianite [21,58–60]. These peaks, together with the broad band near ~3530 cm^{-1}, result from different local cation configurations near OH sites (MgAlOH, AlAlOH and Fe^{3+}AlOH configurations) [58–60]. The band in the 3100–3200 cm^{-1} region is usually assigned to vibrational modes of the OH^- ion in the O(10) site resulting from different local cation configurations [58,60], and is very indistinct. It is either suppressed by unfavorable crystal orientation during the measurement, or it may reflect the incorporation of B into the structure [58]. However, optical properties and microchemical analyses do not suggest boron-enrichment in vesuvianite [61]. The low temperature is in accordance with rodingite formation conditions determined by worldwide fluid inclusions studies [62–64], and thus the temperature yielded by chlorite thermometry roughly represents the temperature under which the latest metasomatic transformation took place.

5.2. Garnet Crystallochemistry

According to chemical composition, no pure end-members of andradite-grossular series were determined. Accordingly, the Raman bands also do not fit with those of pure members and are rather intermediate. The line position corresponds to published wavenumbers for members of ugrandite series garnets [65–69], with bands of SiO_4 rotation and translation modes in the region up to 400 cm^{-1} and with internal (Si-O) bending vibrations at 400–650 cm^{-1}. The frequencies over 800 cm^{-1} are assigned to (Si-O) stretching modes. Raman measurements show the presence of $(OH)^-$ anions in all selected measured points of rodingite garnet zones. Despite the fact that the spectra are affected by increased background, the highest broad-band intensity at ~3600 cm^{-1} is characteristic for grossular-rich zones (Grs 1–3) and for Ti-enriched garnet zones (Ti-Grt 1, 2), whereas younger zones (Adr 1–4) show weak $(OH)^-$ anion signal (Figure 7). Weak and broad features at the frequencies 600–780 cm^{-1} visible in some spectra can also be assigned to rotational modes of the $(OH)^-$ group [66]. The broadening and decrease in intensity of low-frequency spectral bands is characteristic for solid-solution with a decreasing SiO_2 content in grossular (Table 1) and with a suspected increase in $(OH)^-$ (Figure 7, Grs), pronounced in lower sums in EMPA analyses. Titanium presumably substitutes into the octahedrally coordinated *Y*-site. Though those vibrations are Raman inactive, ionic radii of the main *Y*-cations affect the position of the bending vibrations of SiO_4 tetrahedra placed near 510–550 cm^{-1} [65,68,70,71].

Garnet crystallography is a complicated topic due to the mineral's capacity to incorporate a wide range of chemical elements into its structure [16]. In the case of garnet in rodingites from Dobšiná, it comprises a complex calcic solid solution dominated by Al^{3+}, Fe^{3+}, Ti^{4+} and $(OH)^-$ rich end-members. Exact substitution mechanisms are still a matter of discussion [16–18,72], although our analysis of garnet microprobe results can provide some indications. Ca^{2+} solely occupies the *X* cation crystallographic position as the minor deviations of structural formulas from ideal 3 *apfu* probably originated from analytical errors. Other cations, namely Al^{3+}, Fe^{3+} and Ti^{4+}, sum reasonably to about 2 *apfu*, which indicates that dominant substitutions occur at the *Y* crystallographic site. If we considered some of these elements to occupy the *Z*-site, it would mean the presence of a substantial amount of vacancies at *Y* because, in other cases, the normalization would result in an implausible excess of Ca^{2+}. A simple diagram (Figure 9) shows an ideal negative correlation between Al^{3+} and Fe^{3+}+Ti^{4+}; however, such a substitution cannot be easily charge balanced, and therefore some vacancies and/or Fe^{2+} probably need to be considered anyway. Silica deficiency is evident from microprobe results, and Micro-Raman study not only confirms the presence of an $(OH)^-$ anion, but the relative intensity of characteristic bands around 3600 cm^{-1} also proves that less silica means more OH dominated garnet, confirming the known hydrogarnet substitution $(SiO_4)^{4-} \leftrightarrow 4(OH)^-$ [16,73,74]. Unfortunately, reliable spectral quantitative analysis of OH content from thin section samples cannot be easily acquired [19]. Nevertheless, texturally older grossular garnet features this substitution much more than younger andradite rims. Considering the continuous presence of H_2O rich metasomatic fluid during rodingite formation, we can suppose that andradite-richer garnet is less favorable to incorporate an $(OH)^-$ anion into its crystal structure than grossular. Some authors [74,75] suggested a positive correlation between Ti and OH content, but our results indicate that Ti cannot be the sole factor controlling the hydration in garnets.

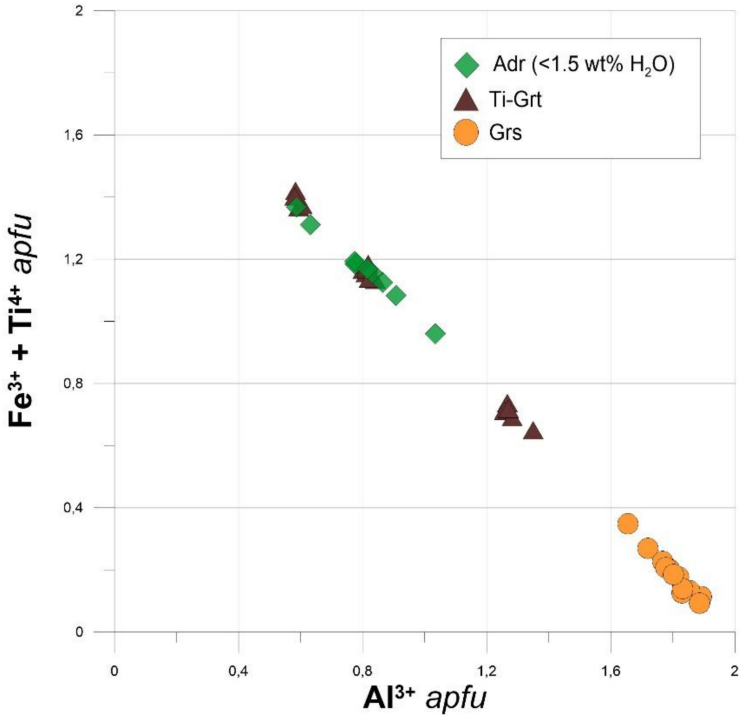

Figure 9. Garnet solid solution chemistry characterized by negative correlation between Al^{3+} and Fe^{3+} + Ti^{4+} at *Y* crystallographic site.

6. Conclusions

Rodingites from serpentinized ultramafic complex in Dobšiná, Western Carpathians, Slovakia, consist of garnet, vesuvianite, diopside and clinochlore. The mineral association can be successively divided into three crystallization stages: 1) diopside relics + possibly older garnet cores; 2) garnet; 3) vesuvianite ± chlorite.

Garnet is represented by a heterogeneous calcic solid solution dominated by grossular, andradite, Ti-rich and OH-rich end-members. Mineral chemistry variation is characterized by ideal negative correlation between Al^{3+} and Fe^{3+} + Ti^{4+}. Ti-garnet possibly represents a chemical signature of an (Fe)-Ti oxide. Older grossular cores are more hydrated compared to younger andradite rims, suggesting that grossular incorporates OH more easily into its structure.

Euhedral vesuvianite crystallizes at the expense of the garnet solid solution. This reaction confirms a high extent of metasomatic transformation, but more research is needed to assign the key factor controlling vesuvianite crystallization in rodingites.

The late metasomatic association of vesuvianite + chlorite formed at a temperature of about 265 °C based on chlorite thermometry models.

Supplementary Materials: The following are available online at https://www.mdpi.com/2075-163X/11/2/189/s1, Table S1: Garnet microprobe analysis and calculated structural formula, Table S2: Vesuvianite microprobe analysis and calculated structural formula, Table S3: Clinopyroxenes microprobe analysis and calculated structural formula, Table S4: Chlorite microprobe analysis and calculated structural formula.

Author Contributions: Conceptualization, J.B. and J.S.; Methodology, J.S. and S.M.; Validation, J.S., S.M.; Gormal analysis, J.B.; Investigation, J.B.; Resources, J.S.; Data curation, J.B. and S.M.; Writing—original draft preparation, J.B.; Writing—review and editing, J.S. and S.M.; Visualization, J.B.; Supervision, J.S.; Project administration, J.S.; Funding acquisition, J.S. All authors have read and agreed to the published version of the manuscript.

Funding: This research was supported by grants VEGA 1/0237/18 and APVV 19-0065.

Data Availability Statement: Data is contained within the article or supplementary material.

Acknowledgments: We thank two anonymous reviewers and the editor for their constructive remarks on the manuscript. We acknowledge T. Mikuš for BSE images and microprobe data acquisition.

Conflicts of Interest: The authors declare no conflict of interest.

References

1. Coleman, R.G. Low-Temperature Reaction Zones and Alpine Ultramafic Rocks of California, Oregon, and Washington. *Geol. Surv. Bull.* **1967**. [CrossRef]
2. Barriga, F.; Fyfe, W.S. Development of Rodingite in Basaltic Rocks in Serpentinites, East Liguria, Italy. *Contr. Mineral. Petrol.* **1983**, *84*, 146–151. [CrossRef]
3. Schandl, E.S.; O'Hanley, D.S.; Wicks, F.J. Rodingites in Serpentinized Ultramafic Rocks of the Abitibi Greenstone Belt, Ontario. *Can. Mineral.* **1989**, *27*, 579–591.
4. Li, X.-P.; Rahn, M.; Bucher, K. Metamorphic Processes in Rodingites of the Zermatt-Saas Ophiolites. *Int. Geol. Rev.* **2004**, *46*, 28–51. [CrossRef]
5. Li, X.-P.; Duan, W.-Y.; Zhao, L.-Q.; Schertl, H.-P.; Kong, F.-M.; Shi, T.-Q.; Zhang, X. Rodingites from the Xigaze Ophiolite, Southern Tibet—New Insights into the Processes of Rodingitization. *Eur. J. Mineral.* **2017**, *29*, 821–837. [CrossRef]
6. El-Shazly, A.K.; Al-Belushi, M. Petrology and Chemistry of Metasomatic Blocks from Bawshir, Northeastern Oman. *Int. Geol. Rev.* **2004**, *46*, 904–938. [CrossRef]
7. Honnorez, J.; Kirst, P. Petrology of Rodingites from the Equatorial Mid-Atlantic Fracture Zones and Their Geotectonic Significance. *Contr. Mineral. Petrol.* **1975**, *49*, 233–257. [CrossRef]
8. Anhaeusser, C.R. Rodingite Occurrences in Some Archaean Ultramafic Complexes in the Barberton Mountain Land, South Africa. *Precambrian Res.* **1979**, *8*, 49–76. [CrossRef]
9. Dubińska, E. Rodingites of the Eastern Part of the Jordanow-Gogolow Serpentinite Massif, Lower Silesia, Poland. *Can. Mineral.* **1995**, *33*, 585–608.
10. Tsikouras, B.; Karipi, S.; Rigopoulos, I.; Perraki, M.; Pomonis, P.; Hatzipanagiotou, K. Geochemical Processes and Petrogenetic Evolution of Rodingite Dykes in the Ophiolite Complex of Othrys (Central Greece). *Lithos* **2009**, *113*, 540–554. [CrossRef]
11. Koutsovitis, P.; Magganas, A.; Pomonis, P.; Ntaflos, T. Subduction-Related Rodingites from East Othris, Greece: Mineral Reactions and Physicochemical Conditions of Formation. *Lithos* **2013**, *172–173*, 139–157. [CrossRef]
12. Ferrando, S.; Frezzotti, M.L.; Orione, P.; Conte, R.C.; Compagnoni, R. Late-Alpine Rodingitization in the Bellecombe Meta-Ophiolites (Aosta Valley, Italian Western Alps): Evidence from Mineral Assemblages and Serpentinization-Derived H_2 -Bearing Brine. *Int. Geol. Rev.* **2010**, *52*, 1220–1243. [CrossRef]
13. Murzin, V.V.; Varlamov, D.A.; Ronkin, Y.L.; Shanina, S.N. Origin of Au-Bearing Rodingite in the Karabash Massif of Alpine-Type Ultramafic Rocks in the Southern Urals. *Geol. Ore Depos.* **2013**, *55*, 278–297. [CrossRef]
14. Tang, Y.; Zhai, Q.-G.; Hu, P.-Y.; Wang, J.; Xiao, X.-C.; Wang, H.-T.; Tang, S.-H.; Lei, M. Rodingite from the Beila Ophiolite in the Bangong–Nujiang Suture Zone, Northern Tibet: New Insights into the Formation Ofophiolite-Related Rodingite. *Lithos* **2018**, *316–317*, 33–47. [CrossRef]
15. Gussone, N.; Austrheim, H.; Westhues, A.; Mezger, K. Origin of Rodingite Forming Fluids Constrained by Calcium and Strontium Isotope Ratios in the Leka Ophiolite Complex. *Chem. Geol.* **2020**, *542*, 119598. [CrossRef]
16. Grew, E.S.; Locock, A.J.; Mills, S.J.; Galuskina, I.O.; Galuskin, E.V.; Halenius, U. Nomenclature of the Garnet Supergroup. *Am. Mineral.* **2013**, *98*, 785–811. [CrossRef]
17. Antao, S.M. Crystal Chemistry of Birefringent Hydrogrossular. *Phys. Chem. Miner.* **2015**, *42*, 455–474. [CrossRef]
18. Schingaro, E.; Lacalamita, M.; Mesto, E.; Ventruti, G.; Pedrazzi, G.; Ottolini, L.; Scordari, F. Crystal Chemistry and Light Elements Analysis of Ti-Rich Garnets. *Am. Mineral.* **2016**, *101*, 371–384. [CrossRef]
19. Geiger, C.A.; Rossman, G.R. IR Spectroscopy and OH– in Silicate Garnet: The Long Quest to Document the Hydrogarnet Substitution. *Am. Mineral.* **2018**, *103*, 384–393. [CrossRef]
20. Panikorovskii, T.; Chukanov, N.; Rusakov, V.; Shilovskikh, V.; Mazur, A.; Balassone, G.; Ivanyuk, G.; Krivovichev, S. Vesuvianite from the Somma-Vesuvius Complex: New Data and Revised Formula. *Minerals* **2017**, *7*, 248. [CrossRef]
21. Galuskin, E.V.; Galuskina, I.O.; Stadnicka, K.; Armbruster, T.; Kozanecki, M. The Crystal Structure of Si-Deficient, OH-Substitued, Boron-Bearing Vesuvianite from Wiluy River, Sakha-Yakutia, Russia. *Can. Mineral.* **2007**, *45*, 239–248. [CrossRef]
22. Groat, L.A.; Evans, R.J.; Cempírek, J.; McCammon, C.; Houzar, S. Fe-Rich and As-Bearing Vesuvianite and Wiluite from Kozlov, Czech Republic. *Am. Mineral.* **2013**, *98*, 1330–1337. [CrossRef]
23. Fitzgerald, S.; Leavens, P.B.; Rossman, G.R.; Yap, G.P.A.; Rose, T. Vesuvianite From Pajsberg, Sweden, and the Role of be in the Vesuvianite Structure. *Can. Mineral.* **2016**, *54*, 1525–1537. [CrossRef]
24. Froitzheim, N.; Plasienka, D.; Schuster, R. Alpine tectonics of the Alps and Western Carpathians. In *The Geology of Central Europe Volume 2: Mesozoic and Cenozoic*; McCann, T., Ed.; The Geological Society of London: London, UK, 2008; pp. 1141–1232. ISBN 978-1-86239-389-9.
25. Plašienka, D.; Grecula, P.; Putiš, M.; Kováč, M.; Hovorka, D. Evolution and structure of the Western Carpathians: An overview. In *Geological Evolution of the Western Carpathians*; Mineralia Slovaca: Monograph; Geological Survey of Slovak Republic: Bratislava, Slovenská, 1997; pp. 1–24.

26. Plašienka, D. Continuity and Episodicity in the Early Alpine Tectonic Evolution of the Western Carpathians: How Large-Scale Processes are Expressed by the Orogenic Architecture and Rock Record Data. *Tectonics* **2018**, *37*, 2029–2079. [CrossRef]
27. Kozur, H. The Evolution of the Meliata-Hallstatt Ocean and Its Significance for the Early Evolution of the Eastern Alps and Western Carpathians. *Palaeogeogr. Palaeoclim. Palaeoecol.* **1991**, *87*, 109–135. [CrossRef]
28. Ivan, P. Relics of Meliata Ocean Crust: Geodynamic Implications of Mineralogical, Petrological and Geochemical Proxies. *Geol. Carpathica* **2002**, *53*, 254–256.
29. Biely, A.; Bezák, V.; Elečko, M.; Gross, P.; Kaličiak, M.; Konečný, V.; Lexa, J.; Mello, J.; Nemčok, J.; Potfaj, M.; et al. Geological Map of Slovakia, 1:500 000 1996. Available online: http://apl.geology.sk/gm50js/ (accessed on 3 November 2020).
30. Hovorka, D.; Ivan, P.; Spišiak, J. Lithology, Petrology, Metamorphism and Tectonic Position of the Klátov Group (Paleozoic of the Gemer Unit, Inner Western Carpathians). *Acta Geol. Geogr. Univ. Comen. Geol.* **1990**, *45*, 55–69.
31. Hovorka, D.; Ivan, P.; Jaroš, J.; Kratochvíl, M.; Reichwalder, P.; Rojkovič, I.; Spišiak, J.; Turanová, L. *Ultramafic Rocks of the Western Carpathians/Czechoslovakia*; GÚDŠ: Bratislava, Slovenská, 1985.
32. Fediuková, E.; Hovorka, D.; Greguš, J. Compositional Zoning of Andradite from Serpentinite at Dobsina (West Carpathians). *Věst. Ústř. Úst. Geol.* **1976**, *51*, 339–345.
33. Putiš, M.; Koppa, M.; Snárska, B.; Koller, F.; Uher, P. The Blueschist-Associated Perovskite-Andradite-Bearing Serpentinized Harzburgite from Dobšiná (the Meliata Unit), Slovakia. *J. Geosci.* **2012**, *57*, 221–240. [CrossRef]
34. Putiš, M.; Yang, Y.-H.; Vaculovič, T.; Koppa, M.; Li, X.-H.; Uher, P. Perovskite, Reaction Product of a Harzburgite with Jurassic–Cretaceous Accretionary Wedge Fluids (Western Carpathians, Slovakia): Evidence from the Whole-Rock and Mineral Trace Element Data. *Geol. Carpathica* **2016**, *67*, 135–148. [CrossRef]
35. Li, X.-H.; Putiš, M.; Yang, Y.-H.; Koppa, M.; Dyda, M. Accretionary Wedge Harzburgite Serpentinization and Rodingitization Constrained by Perovskite U/Pb SIMS Age, Trace Elements and Sm/Nd Isotopes: Case Study from the Western Carpathians, Slovakia. *Lithos* **2014**, *205*, 1–14. [CrossRef]
36. Yavuz, F.; Kumral, M.; Karakaya, N.; Karakaya, M.Ç.; Yıldırım, D.K. A Windows Program for Chlorite Calculation and Classification. *Comput. Geosci.* **2015**, *81*, 101–113. [CrossRef]
37. Morimoto, N. Nomenclature of Pyroxenes. *Bull. Minéralogie* **1988**, *111*, 535–550. [CrossRef]
38. Bøe, R. Rodingite from Lindås, Western Norway. *Norsk Geol. Tidsskr.* **1985**, *65*, 301–320.
39. Piber, A.; Tropper, P. Ba-Ti-Bearing Metarodingites from the Austroalpine Units (Innsbruck Quartzphyllite, Wildschönau Schists) North of the Tauern Window (Tyrol, Eastern Alps, Austria). *N. Jb. Miner. Abh.* **2010**, *187*, 189–205. [CrossRef]
40. Python, M.; Yoshikawa, M.; Shibata, T.; Arai, S. Diopsidites and Rodingites: Serpentinisation and Ca-Metasomatism in the Oman Ophiolite Mantle. In *Dyke Swarms: Keys for Geodynamic Interpretation*; Springer: Berlin/Heidelberg, Germany, 2011; pp. 401–435. ISBN 978-3-642-12495-2.
41. Koutsovitis, P. High-Pressure Subduction-Related Serpentinites and Metarodingites from East Thessaly (Greece): Implications for Their Metamorphic, Geochemical and Geodynamic Evolution in the Hellenic–Dinaric Ophiolite Context. *Lithos* **2017**, *276*, 122–145. [CrossRef]
42. Li, X.-P.; Zhang, L.; Wei, C.; Ai, Y.; Chen, J. Petrology of Rodingite Derived from Eclogite in Western Tianshan, China. *J. Metamorph. Geol.* **2007**, *25*, 363–382. [CrossRef]
43. Tsikouras, B.; Karipi, S.; Hatzipanagiotou, K. Evolution of Rodingites along Stratigraphic Depth in the Iti and Kallidromon Ophiolites (Central Greece). *Lithos* **2013**, *175–176*, 16–29. [CrossRef]
44. Li, X.-P.; Rahn, M.; Bucher, K. Eclogite Facies Metarodingites—Phase Relations in the System SiO_2-Al_2O_3-Fe_2O_3-FeO-MgO-CaO-CO_2-H_2O: An Example from the Zermatt-Saas Ophiolite. *J. Metamorph. Geol.* **2008**, *26*, 347–364. [CrossRef]
45. Salvioli-Mariani, E.; Boschetti, T.; Toscani, L.; Montanini, A.; Petriglieri, J.R.; Bersani, D. Multi-Stage Rodingitization of Ophiolitic Bodies from Northern Apennines (Italy): Constraints from Petrography, Geochemistry and Thermodynamic Modelling. *Geosci. Front.* **2020**, *11*, 2103–2125. [CrossRef]
46. Zanoni, D.; Rebay, G.; Spalla, M.I. Ocean Floor and Subduction Record in the Zermatt-Saas Rodingites, Valtournanche, Western Alps. *J. Metamorph. Geol.* **2016**, *34*, 941–961. [CrossRef]
47. Rice, J.M. Metamorphism of Rodingites: Part I. Phase Relations in a Portion of the System CaO-MgO-Al2O3-SiO2-CO2-H2O. *Am. J. Sci.* **1983**, *283*, 121–150.
48. Galuskin, E.V.; Armbruster, T.; Malsy, A.; Galuskina, I.O.; Sitarz, M. Morphology, Composition and Structure of Low-Temperature P4/Nnc High-Fluorine Vesuvianite Whiskers from Polar Yakutia, Russia. *Can. Mineral.* **2003**, *41*, 843–856. [CrossRef]
49. Puschnig, A.R. Metasomatic Alterations at Mafic-Ultramafic Contacts in Valmalenco (Rhetic Alps, N-Italy). *Schweiz. Mineral. Petrogr. Mitt.* **2002**, *82*, 515–536.
50. Hatzipanagiotou, K.; Tsikouras, B.; Migiros, G.; Gartzos, E.; Serelis, K. Origin of Rodingites in Ultramafic Rocks from Lesvos Island (NE Aegean, Greece). *Ofioliti* **2003**, *28*, 13–23.
51. Pomonis, P.; Tsikouras, B.; Karipi, S.; Hatzipanagiotou, K. Rodingite Formation in Ultramafic Rocks from the Koziakas Ophiolite, Western Thessaly, Greece: Conditions of Metasomatic Alteration, Geochemical Exchanges and T-X(CO2) Evolutionary Path. *Can. Mineral.* **2008**, *46*, 569–581. [CrossRef]
52. Austrheim, H.; Prestvik, T. Rodingitization and Hydration of the Oceanic Lithosphere as Developed in the Leka Ophiolite, North–Central Norway. *Lithos* **2008**, *104*, 177–198. [CrossRef]

53. Hu, C.-N.; Santosh, M. Devonian Rodingite from the Northern Margin of the North China Craton: Mantle Wedge Metasomatism during Ocean-Continent Convergence. *Int. Geol. Rev.* **2018**, *60*, 1073–1097. [CrossRef]
54. Koutsovitis, P.; Magganas, A.; Ntaflos, T.; Koukouzas, N. Rodingitization and Carbonation, Associated with Serpentinization of Triassic Ultramafic Cumulates and Lavas in Othris, Greece. *Lithos* **2018**, *320–321*, 35–48. [CrossRef]
55. Laborda-López, C.; López-Sánchez-Vizcaíno, V.; Marchesi, C.; Gómez-Pugnaire, M.T.; Garrido, C.J.; Jabaloy-Sánchez, A.; Padrón-Navarta, J.A.; Hidas, K. High- *P* Metamorphism of Rodingites during Serpentinite Dehydration (Cerro Del Almirez, Southern Spain): Implications for the Redox State in Subduction Zones. *J. Metamorph. Geol.* **2018**, *36*, 1141–1173. [CrossRef]
56. Paluszkiewicz, C.; Żabiński, W. Vibrational Spectroscopy as a Tool for Discrimination of High and Low Vesuvianite. *Vib. Spectrosc.* **2004**, *35*, 77–80. [CrossRef]
57. Dumańska-Słowik, M.; Powolny, T.; Khac, G.N.; Heflik, W.; Sikorska-Jaworowska, M. Petrogenesis of Scapolite-Rich Gabbro from the Alkaline Cho Don Complex in North-Eastern Vietnam—Mineralogical and Geochemical Implications. *Lithos* **2020**, *374–375*, 105703. [CrossRef]
58. Groat, L.A.; Hawthorne, F.C.; Rossman, G.R.; Ercit, T.S. The Infrared Spectroscopy of Vesuvianite in the OH Region. *Can. Mineral.* **1995**, *3*, 609–626.
59. Borovikova, E.Y.; Kurazhkovskaya, V.S. Infrared Spectra and Factor Group Analysis of Vesuvianites in OH Region. *Vib. Spectrosc.* **2005**, *39*, 95–98. [CrossRef]
60. Galuskin, E.V.; Janeczek, J.; Kozanecki, M.; Sitarz, M.; Jastrzębski, W.; Wrzalik, R.; Stadnicka, K. Single-Crystal Raman Investigation of Vesuvianite in the OH Region. *Vib. Spectrosc.* **2007**, *44*, 36–41. [CrossRef]
61. Groat, L.A.; Hawthorne, F.C.; Ercit, T.S. The Chemistry of Vesuvianite. *Can. Mineral.* **1992**, *30*, 19–48.
62. Mittwede, S.K.; Schandl, E.S. Rodingites from the Southern Appalachian Piedmont, South Carolina, USA. *EJM* **1992**, *4*, 7–16. [CrossRef]
63. Dubińska, E.; Bylina, P.; Kozłowski, A.; Dörr, W.; Nejbert, K.; Schastok, J.; Kulicki, C. U–Pb Dating of Serpentinization: Hydrothermal Zircon from a Metasomatic Rodingite Shell (Sudetic Ophiolite, SW Poland). *Chem. Geol.* **2004**, *203*, 183–203. [CrossRef]
64. Normand, C.; Williams-Jones, A.E. Physicochemical Conditions and Timing of Rodingite Formation: Evidence from Rodingite-Hosted Fluid Inclusions in the JM Asbestos Mine, Asbestos, Québec. *Geochem. Trans.* **2007**, *8*, 11. [CrossRef] [PubMed]
65. Kolesov, B.A.; Geiger, C.A. Raman Spectra of Silicate Garnets. *Phys. Chem. Min.* **1998**, *25*, 142–151. [CrossRef]
66. Kolesov, B.A.; Geiger, C.A. The Vibrational Spectrum of Synthetic Hydrogrossular (Katoite) Ca3Al2(O4H4)3: A Low-Temperature IR and Raman Spectroscopic Study. *Am. Mineral.* **2005**, *90*, 1335–1341. [CrossRef]
67. Arredondo, E.H.; Rossman, G.R. Feasibility of Determining the Quantitative OH Content of Garnets with Raman Spectroscopy. *Am. Mineral.* **2002**, *87*, 307–311. [CrossRef]
68. Uher, P.; Milovská, S.; Milovský, R.; Koděra, P.; Bačík, P.; Bilohuščin, V. Kerimasite, $\{Ca_3\}[Zr_2](SiFe^{3+}{}_2)O_{12}$ Garnet from the Vysoká-Zlatno Skarn, Štiavnica Stratovolcano, Slovakia. *Mineral. Mag.* **2015**, *79*, 715–733. [CrossRef]
69. Bersani, D.; Andò, S.; Vignola, P.; Moltifiori, G.; Marino, I.-G.; Lottici, P.P.; Diella, V. Micro-Raman Spectroscopy as a Routine Tool for Garnet Analysis. *Spectrochim. Acta Part A Mol. Biomol. Spectrosc.* **2009**, *73*, 484–491. [CrossRef]
70. Pinet, M.; Smith, D.C. La microspectrométrie Raman des grenats X3Y2Z3O12. I, La série calcique naturelle ouvarovite-grossulaire-andradite = Raman microspectometry of garnets X3Y2Z3O12. I, The natural calcic series uvarovite-grossular-andradite. *Schweiz. Mineral. Petrogr. Mitt.* **1993**, *73*, 21–40. [CrossRef]
71. Galuskina, I.O.; Galuskin, E.V.; Lazic, B.; Armbruster, T.; Dzierżanowski, P.; Prusik, K.; Wrzalik, R. Eringaite, $Ca_3Sc_2(SiO_4)_3$, a New Mineral of the Garnet Group. *Mineral. Mag.* **2010**, *74*, 365–373. [CrossRef]
72. Schmitt, A.C.; Tokuda, M.; Yoshiasa, A.; Nishiyama, T. Titanian Andradite in the Nomo Rodingite: Chemistry, Crystallography, and Reaction Relations. *J. Mineral. Petrol. Sci.* **2019**, *114*, 111–121. [CrossRef]
73. Rossman, G.R.; Aines, R.D. The Hydrous Components in Garnets: Grossular-Hydrogrossular. *Am. Mineral.* **1991**, *76*, 1153–1164.
74. Amthauer, G.; Rossman, G.R. The Hydrous Component in Andradite Garnet. *Am. Mineral.* **1998**, *83*, 835–840. [CrossRef]
75. Peslier, A.H. A Review of Water Contents of Nominally Anhydrous Natural Minerals in the Mantles of Earth, Mars and the Moon. *J. Volcanol. Geotherm. Res.* **2010**, *197*, 239–258. [CrossRef]